Supporting Information

1. Experimental section

Separator Materials and Sources

Three commercial separators with distinct microstructures were used in this study: glass fibre (GF, 150μm, Whatman), polypropylene (PP, Celgard 2400, 25 μm), and cellulose paper (CP, Whatman, 28–30 μm). All separators were used as received unless otherwise specified. Prior to assembly, separators were vacuum-dried at 60 °C for 12 h to remove residual moisture and stored in a desiccator. Detailed structural and physicochemical properties of each separator, including porosity, tortuosity, air permeability, electrolyte uptake, and wetting behaviour, are provided in the Supplementary Information.

Cell Assembly

Pouch and prismatic cells used VO_2 (Zhejiang Vastech Co., Ltd) cathodes (8:1:1, VO_2: carbon:PVDF) coated on stainless-steel foil (7 mg cm^{-2}), cut into 15 × 13 cm sheets. The electrodes were stacked, vacuum-sealed, and injected with electrolyte, followed by a 6 h rest to ensure full wetting.

Operando X-ray Computed Tomography (X-CT)

Operando X-CT was conducted using a customised 1/8″ PFA Swagelok cell with a Ti|Zn configuration to minimise beam attenuation at the Zn–separator interface. Time-resolved scans captured gas evolution, bubble–metal interactions, and interfacial morphological changes during cycling. CT datasets were reconstructed and segmented to quantify porosity, interfacial thickness, and gas-accumulation dynamics.

Materials and Electrochemical Characterisation

SEM (JEOL JSM-6701F), TEM (JEOL JEM-2100), XPS (Thermo K-Alpha), FTIR (Shimadzu IRTracer-100), Raman (DXR3, 532 nm), optical microscopy (Keyence VXH-7000N), FIB-SEM/EDS (Helios G4), AFM (Bruker Dimension Icon), IC (ICS-5000), and ICP-OES (Agilent 5110) were conducted using standard procedures. Electrochemical tests used NEWARE, BioLogic VMP-3 (CV), and Gamry Interface 1000E (EIS).

2. Incidence and bibliography analysis

Statistical and bibliometric analyses were performed to assess the overlooked role of gas bubbles in battery failures. Incident data (2006-2024) were sourced from safety authority reports, insurance databases, recall notices, and peer-reviewed case studies. Causes were

manually classified and cross-validated, with gas-related events defined as swelling, venting, SEI-gas release, or plating-induced gas pockets. Bibliometric data were retrieved from Web of Science, Scopus, and Dimensions using Boolean queries linking gas evolution with battery failure. Publication trends were normalized to total battery-safety outputs, and keyword and co-citation analyses were conducted using CiteSpace. Findings show a clear mismatch: gas-evolution mechanisms account for >25% of severe failures but receive less research attention.

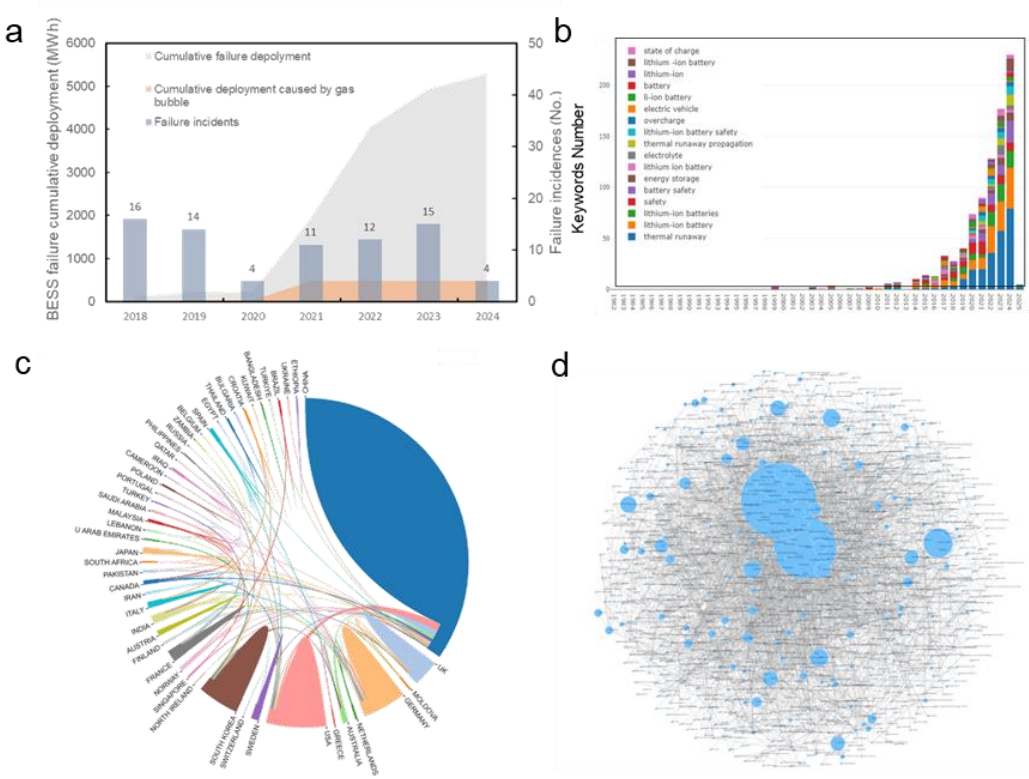

Figure S1. Bibliometric analyses identify gas bubbles as a critical yet overlooked driver of battery failure. (a) Global incident records (2006–2024) from public databases, regulatory reports, and insurance summaries show that gas-evolution-related degradation accounts for >25% of catastrophic failures, with higher incidence in large-format systems. (b) A literature survey (Web of Science) using targeted keywords reveals that, despite rapid growth in battery-safety publications, gas-bubble studies represent <5% of total output. (c) Chord analysis of text-mined incident reports and safety white papers shows strong co-occurrence of gas evolution with electrolyte decomposition, thermal escalation, and mechanical deformation. (d) Co-citation mapping shows fragmented research with limited integration across electrochemistry, fluid dynamics, and safety engineering.

3. Risks and Costs Across the Three Phases of Bubble Evolution

Gas-bubble evolution during battery operation can be classified into three phases with distinct impacts. The early phase involves minor gas formation, negligible performance loss, and only routine inspection costs. In the intermediate phase, bubble accumulation causes measurable degradation, which can be quantified by correlating activation overpotential with bubble density from prior studies. The terminal phase leads to swelling, rupture, or thermal runaway, where total economic losses-including replacement and collateral damage-must be evaluated using 2024 industry data. As shown in Figure 1, cost-loss increases modestly from early to intermediate (~20%) but surges in the terminal phase to 378.95% (3-4 times battery value). This escalation highlights the need for early detection and phase-specific intervention.

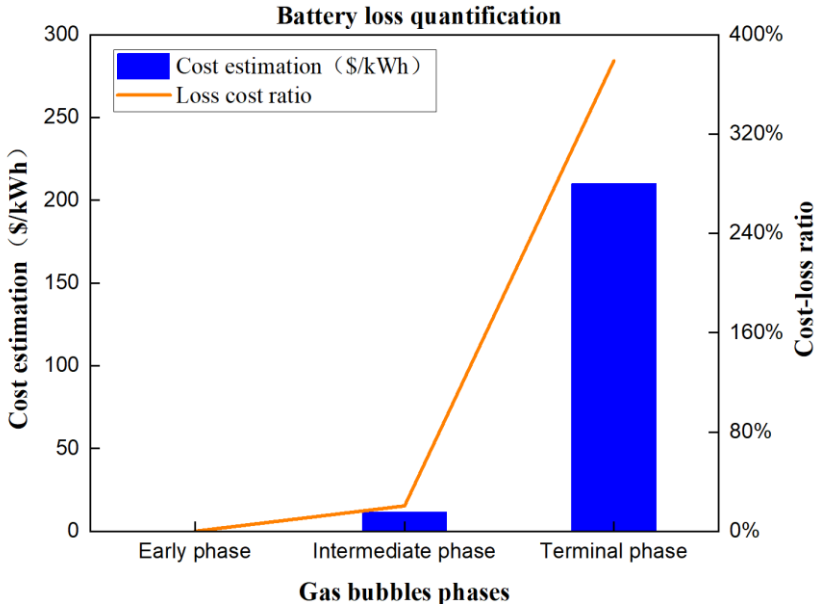

Figure S2. Battery loss cost estimation

4. *In-situ* optical microscopy

In-situ optical microscopy was employed to directly visualize the interfacial gas-bubble evolution during battery operation. The imaging reveals a three-stage progression.

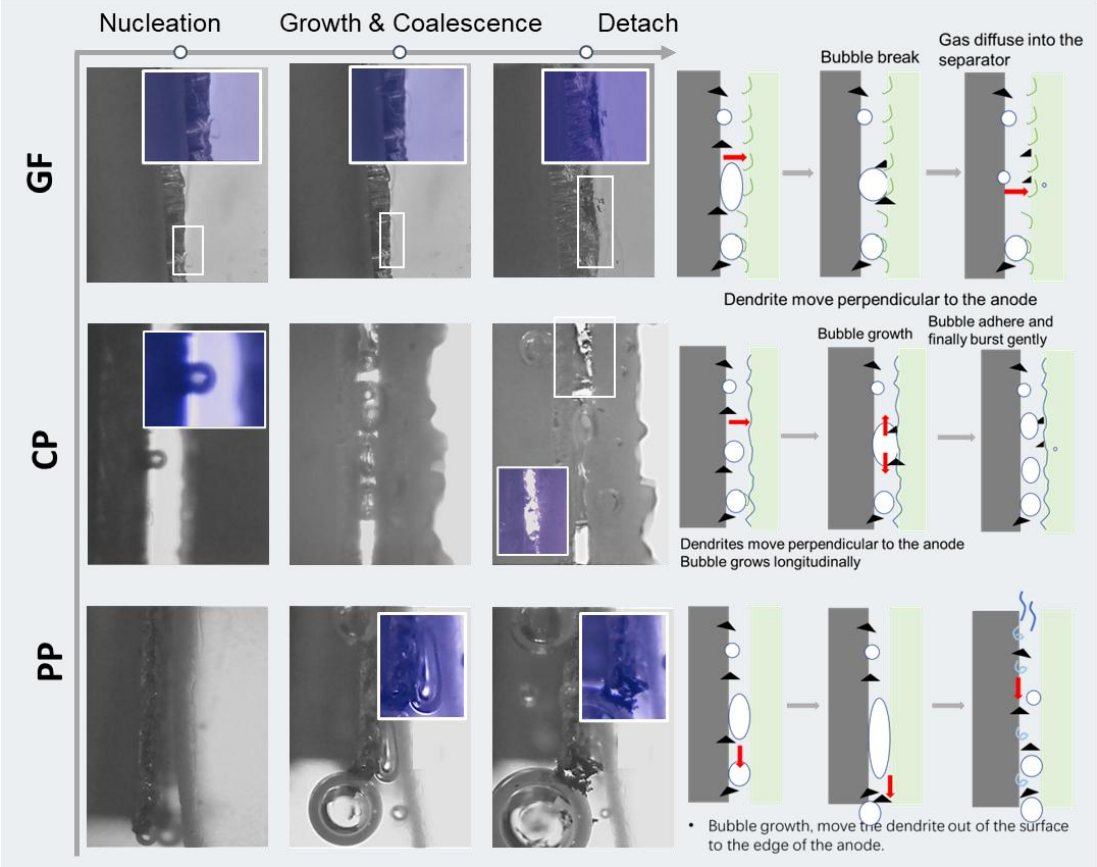

Figure S3. *In-situ* optical observation for three different interfacial separators: GF, PP and CP.

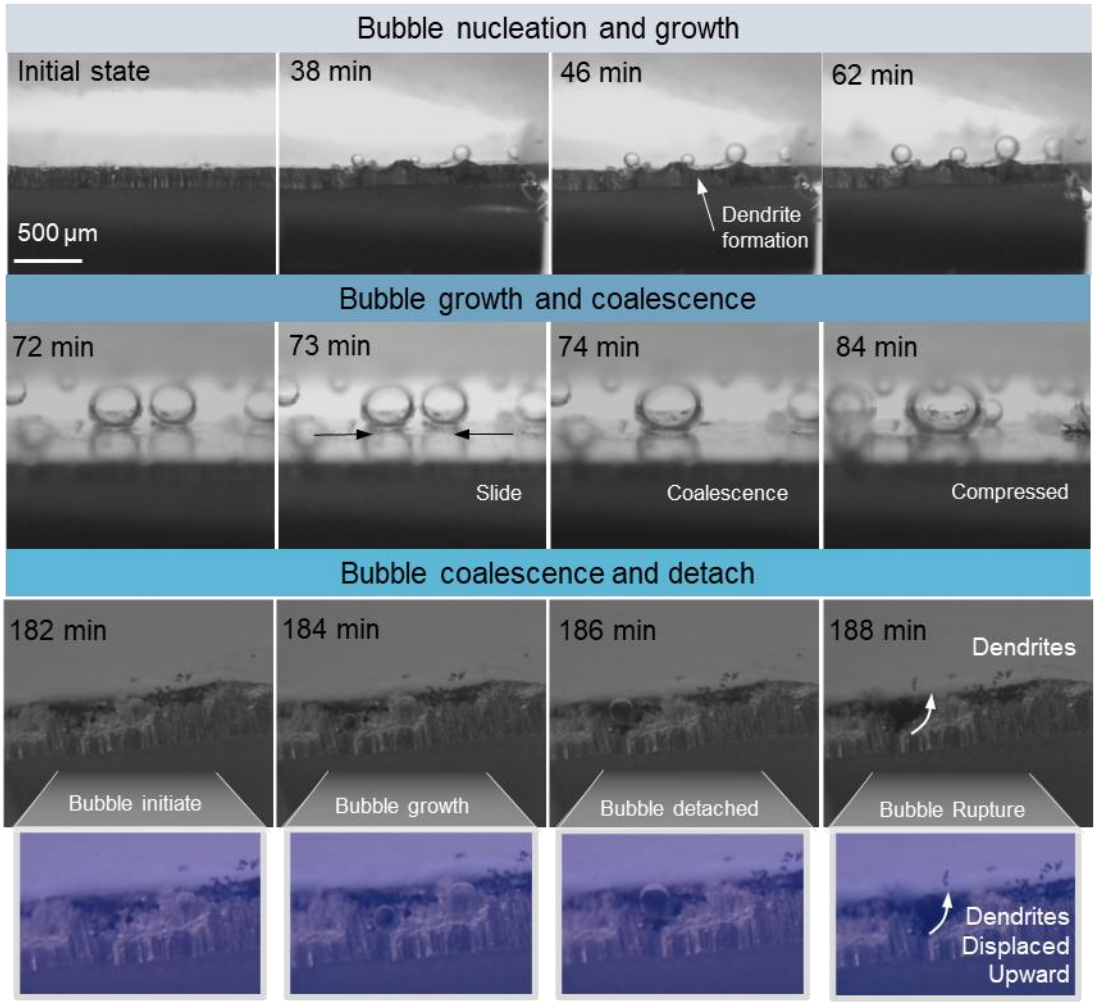

Figure S4. Detailed *In-situ* optical observation for glass fibre separator (GF)

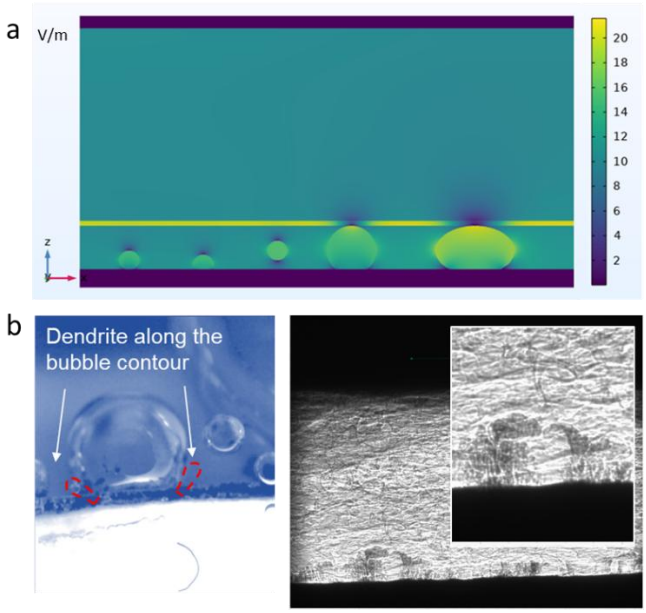

Figure S5 (a) Electric field simulations. (b) optical and CT image observations confirm dendrite growth guided along this bubble contour.

5. Material characterisations of separators

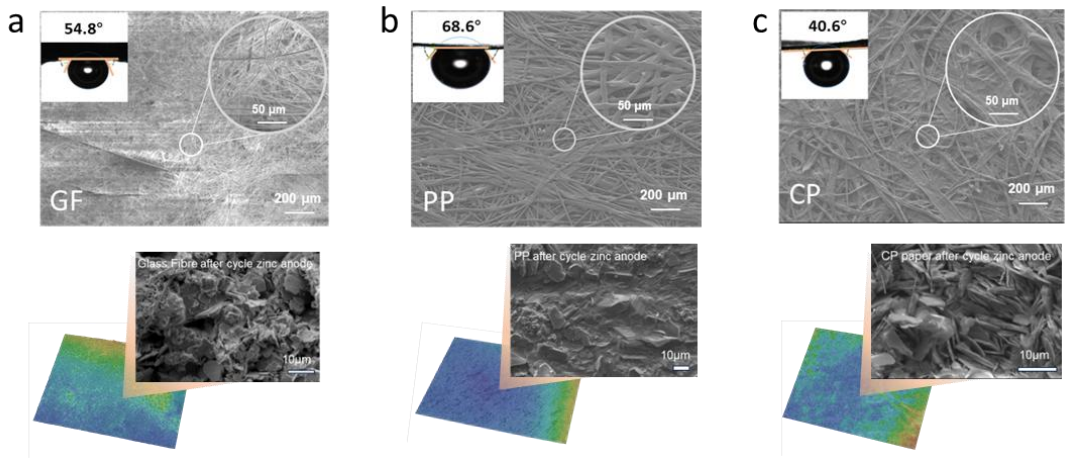

Figure S6. Surface morphology, wettability, and post-cycling structure of zinc anodes paired with GF, PP, and CP separators. Top: SEM images revealing distinct ion transport pathways across glass fiber (GF), polypropylene (PP), and cellulose paper (CP) separators, accompanied by corresponding bubble contact angles (54.8°, 68.6°, and 40.6°), indicating differences in electrolyte affinity. Middle insets: High-magnification SEM images of Zn anode surfaces after cycling show smooth deposition for GF, uneven and dendritic deposits for PP, and compact lamellar deposits for CP. Bottom: 3D surface maps qualitatively illustrate the variation in microstructural uniformity induced by each separator.

6. *Operando* X-ray CT

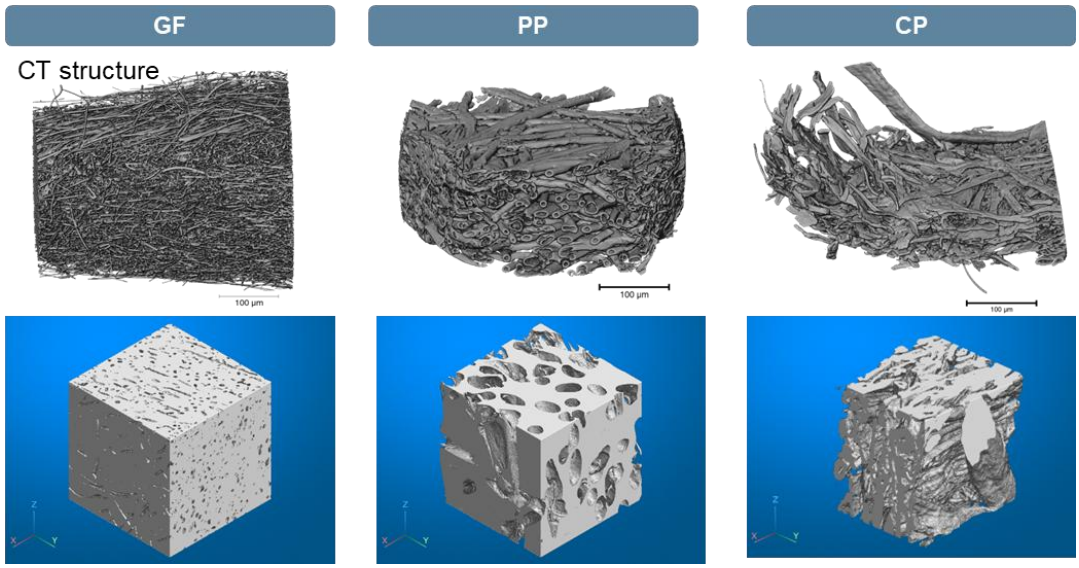

Figure S7. 3D X-ray CT reconstruction and pore-network models of GF, PP, and CP separators.

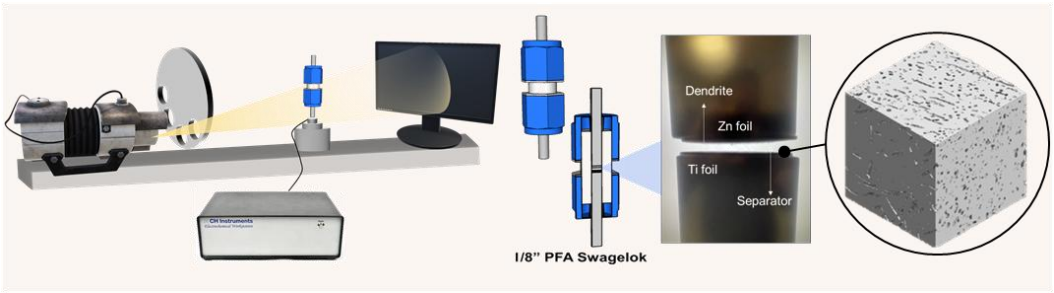

Figure S8. *Operando* X-ray CT setup and cell configuration for visualizing Zn deposition through separators. Schematic of the operando X-ray computed tomography (CT) platform used to track Zn deposition and dendrite evolution during cycling. A customised 1/8″ PFA Swagelok cell enables X-ray transparency while accommodating a Ti|Zn configuration with the separator positioned between the electrodes. The setup allows real-time 3D imaging of the electrode–separator interface, providing direct insight into microstructural evolution under operating conditions.

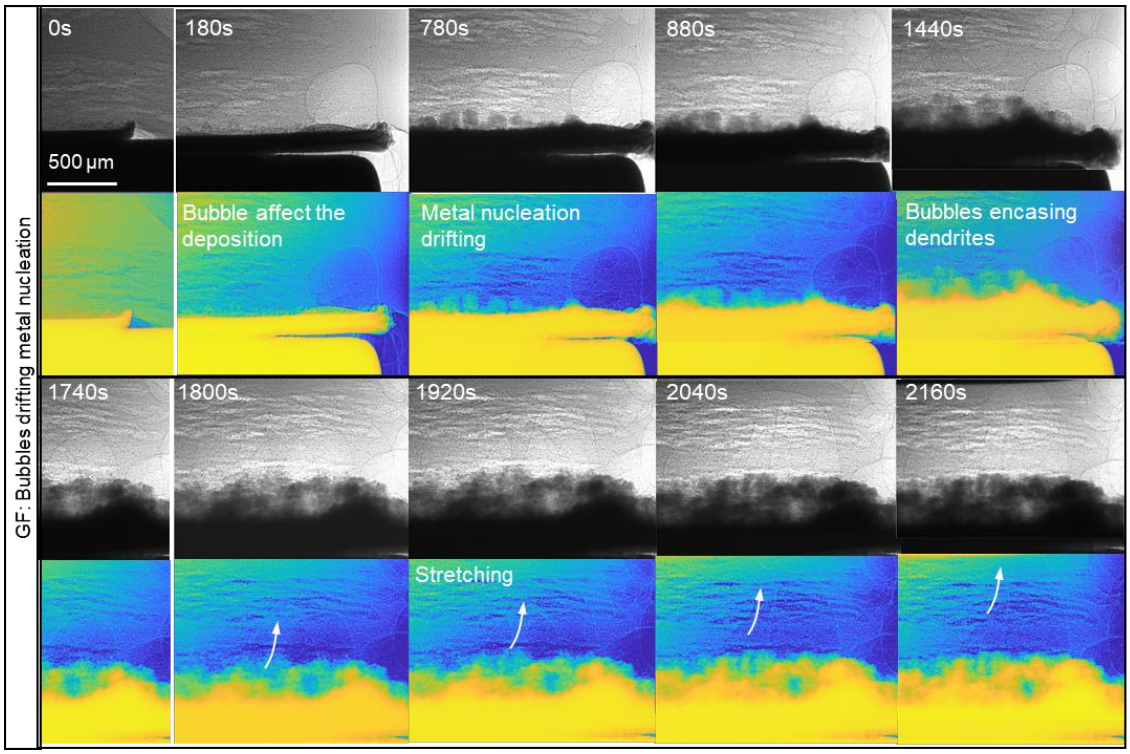

Figure S9. *Operando* CT visualization of bubble–metal interaction for GF

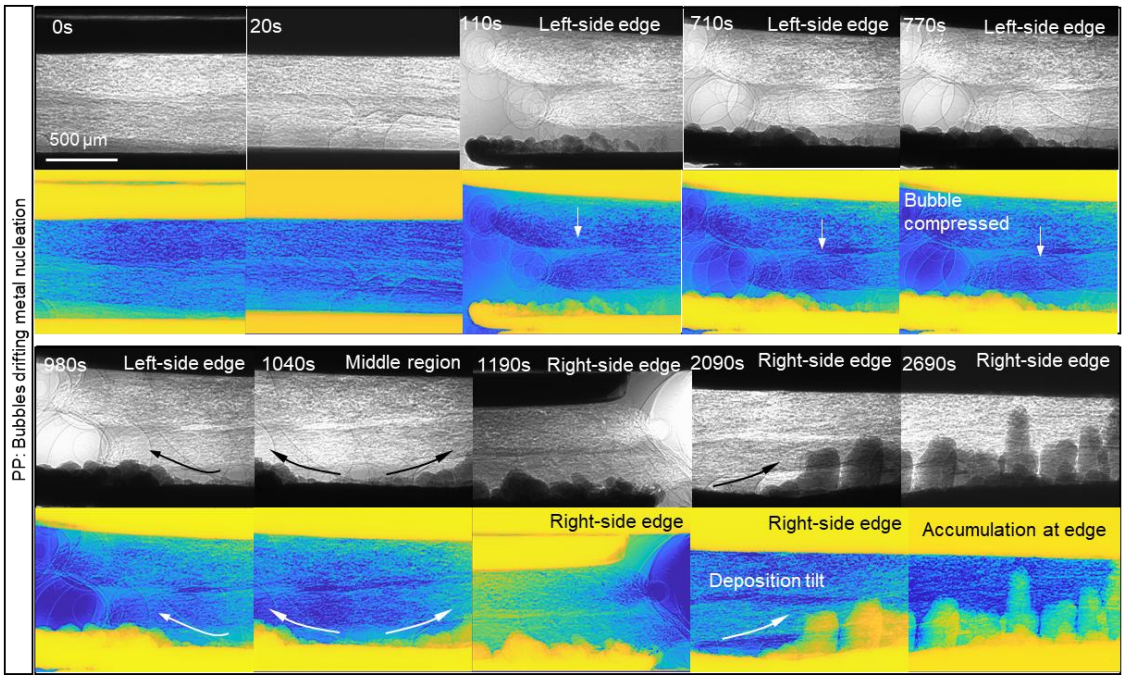

Figure S10. *Operando* CT visualization of bubble–metal interaction for PP

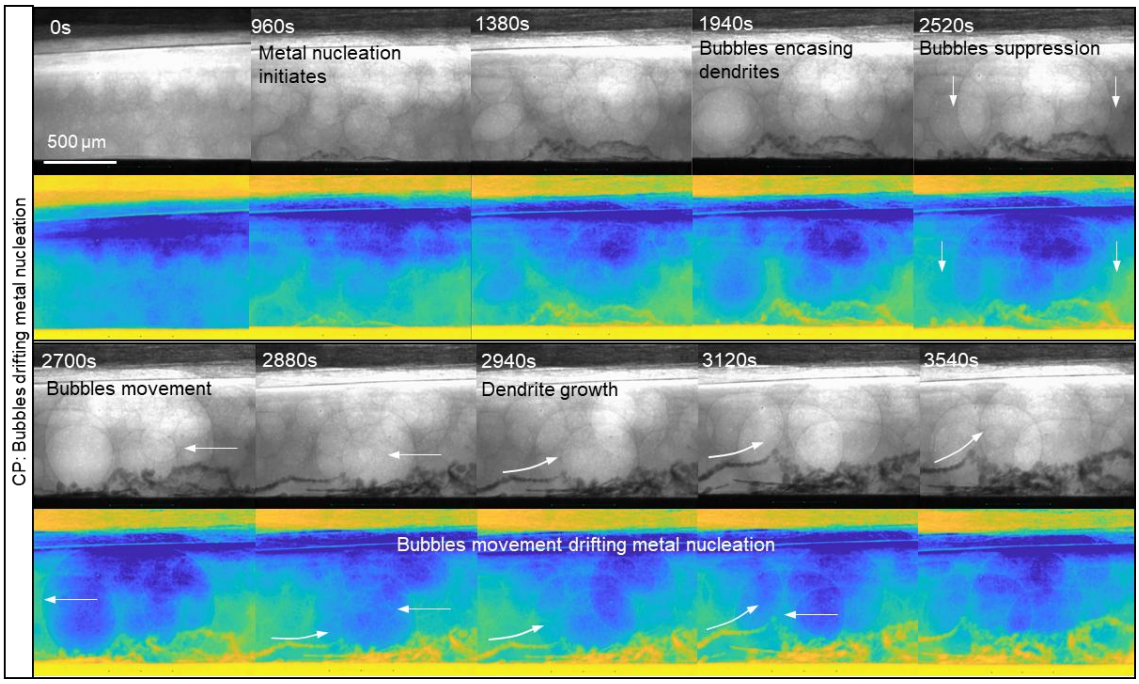

Figure S11. *Operando* CT visualization of bubble–metal interaction for CP

7. CFD simulation

To resolve the time-dependent gas bubble distribution within the separator microstructure and quantify the development of preferential transport pathways during electrodeposition. The 3D geometry of the separator was obtained from X-ray CT. A representative volume element (RVE) was extracted and segmented into pore and solid domains using a threshold-based algorithm.

The extracted sub-volume was meshed for finite-element analysis. Gas transport through the electrolyte-filled porous medium was modelled using a transient convection–diffusion formulation coupled with phase-field treatment of gas–liquid interfaces:

$$\frac{\partial C_g}{\partial t} = D_g \nabla^2 C_g - \nabla \cdot (C_g \mathbf{u})$$

where C_g is gas concentration, D_g is gas diffusivity in the electrolyte, and $\mathbf{u}$ is the liquid velocity field.

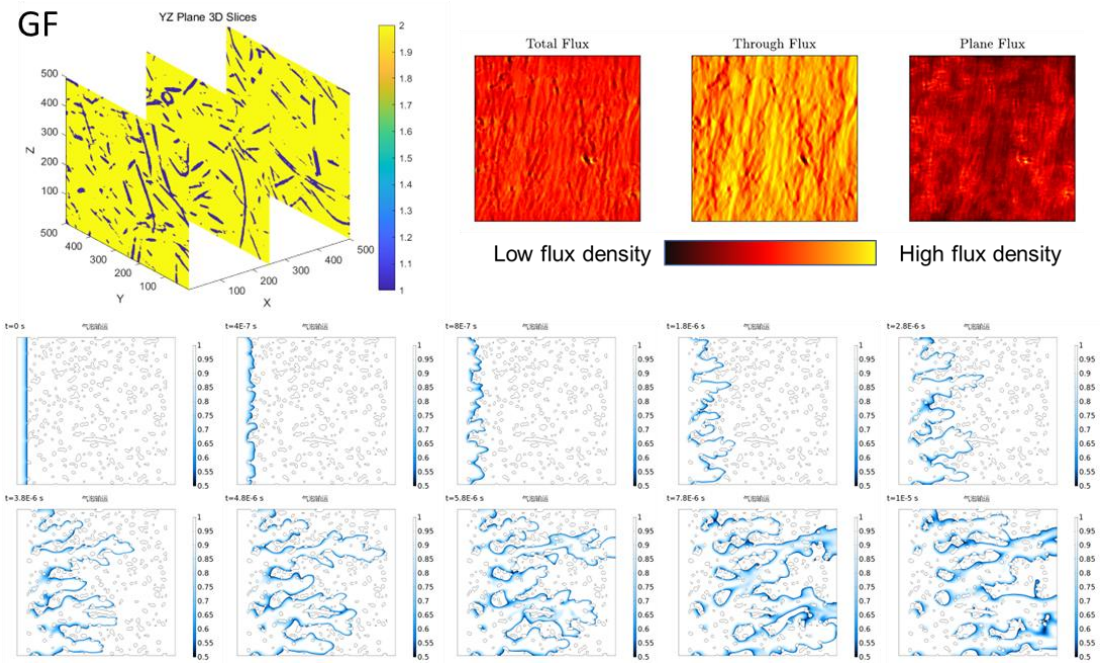

Figure S12. CFD simulation of gas transport and evolution within the GF separator microstructure.

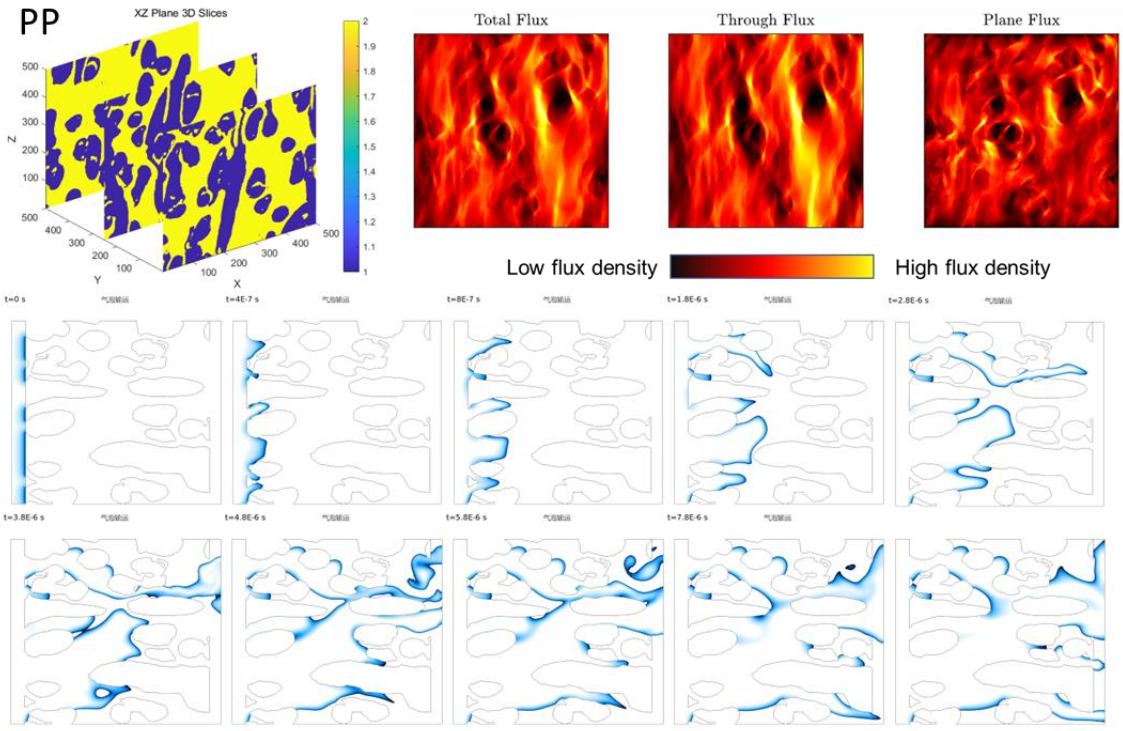

Figure S13. CFD simulation of gas transport and evolution within the PP separator microstructure.

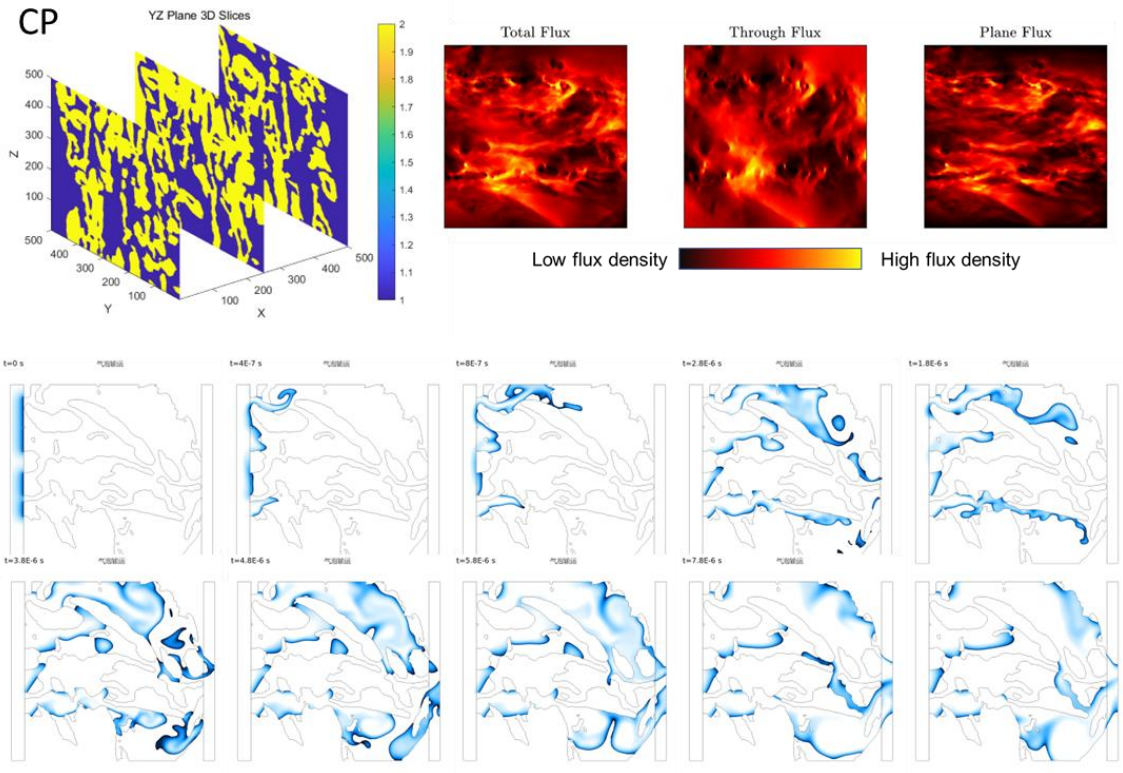

Figure S14. CFD simulation of gas transport and evolution within the CP separator microstructure.

8. Explainable programing

To quantitatively formulate this mechanism, we employed an explainable symbolic regression framework to derive the explicit analytical form of $J_{gas-transport}$ directly from operando data, rather than relying on empirical curve fitting. The algorithm was designed to constrain the search space to physically meaningful expressions by incorporating 7 parameters known to influence gas-interrupted ion transport, as shown in Table S1. Over 60 candidate functional forms were generated by systematically combining these variables with dimensionless constants while enforcing physical constraints (e.g., monotonicity, non-negativity, and correct limiting behaviors for $f_g \to 0$and $t \to 0$). This approach revealed that the contribution of gas transport follows a time-scaling law, where the early-stage growth of gas obstruction is governed by a diffusion-like $t^{1/2}$dependence. The regression first yielded a full symbolic form:

$$J_{gas-transport} = \frac{e^{-a_4/a_2} \cdot \min\left(0.962t^{1/2}, t/(a_6 a_2^2)\right)}{\max\left(1.225, \min\left(a_4, a_5 - 2.337\right)\right)}$$

which captures the competition between gas-induced tortuosity buildup and ion transport relaxation.

Direction	GF		PP		FP	
	Deff (m^2 s^{-1})	Tortuosity factor	Deff (m^2 s^{-1})	Tortuosity factor	Deff (m^2 s^{-1})	Tortuosity factor
1	0.786	1.12	0.399	1.45	0.0907	5.95
2	0.766	1.15	0.328	1.76	0.34	1.59
3	0.791	1.11	0.439	1.31	0.306	1.76
mean	0.781	1.13	0.389	1.51	0.246	3.10
max	0.791	1.15	0.439	1.76	0.34	5.95
min	0.766	1.11	0.328	1.31	0.0907	1.59
	a_0			t		
	a_1			D_{eff}_mean		
	a_2			D_{eff}_max		
	a_3			D_{eff}_min		
	a_4			T_mean		
	a_5			T_max		
	a_6			T_min		

Table S1. Seven parameters used in functions

To improve interpretability and generalizability, the expression was further reduced to a compact form:

$$J_{gas-transport} = C_{gas-transport} \cdot t^{1/2}$$

where $C_{gas-transport}$ is the explainable coupling coefficient that quantitatively reflects the dynamic interaction strength between interfacial gas flux, ion migration, and evolving microstructure. Notably, $C_{gas-transport}$ increases with higher tortuosity and reduced D_e,

consistent with physical intuition that interconnected gas domains impose growing transport resistance over time. After a characteristic time t_c, the contribution transitions into a diffusion-controlled $t^{1/2}$ scaling, in agreement with the temporal evolution of bubble growth, coalescence, and rupture observed experimentally.

GF	$y = exp(-1.4285) * 1.449 * \mathrm{t}/1.225, \mathrm{t} \leq 0.441$
	$y = exp(-1.4285) * 0.962t^{1/2}/1.225, t > 0.441$
PP	$y = exp(-3.4396) * 3.962 * \mathrm{t}/1.225, \mathrm{t} \leq 0.0589$
	$y = exp(-3.4396) * 0.962t^{1/2}/1.225, t > 0.0589$
CP	$y = exp(-9.117) * 5.44 * \mathrm{t}/3.1, \mathrm{t} \leq 0.031$
	$y = exp(-9.117) * 0.962t^{1/2}/3.1, t > 0.031$

Table S2 Candidate functions with detailed coefficients, where t denotes the normalized plating time

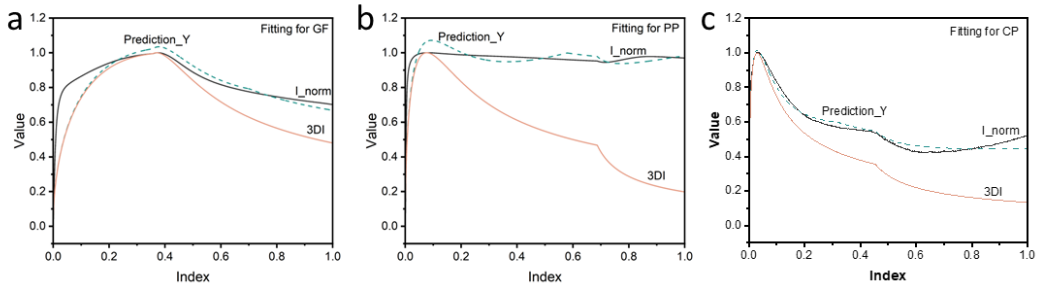

Figure S15. Symbolic regression fitting of experimental current–time profiles for different separators.

This symbolic model accurately reproduces the experimental current–time evolution (Figure 4d) and decouples the gas-driven current component from the intrinsic Scharifker–Hills term, confirming that interfacial gas transport is not a parasitic side effect but an *active and quantifiable* kinetic contributor. Beyond regression accuracy, the explicit analytical form provides mechanistic interpretability—clarifying how gas accumulation transitions the system from 2D interfacial plating toward 3D dendritic growth, and why timely gas rupture (as in GF) restores 2D deposition stability.

9. Prismatic cell performance

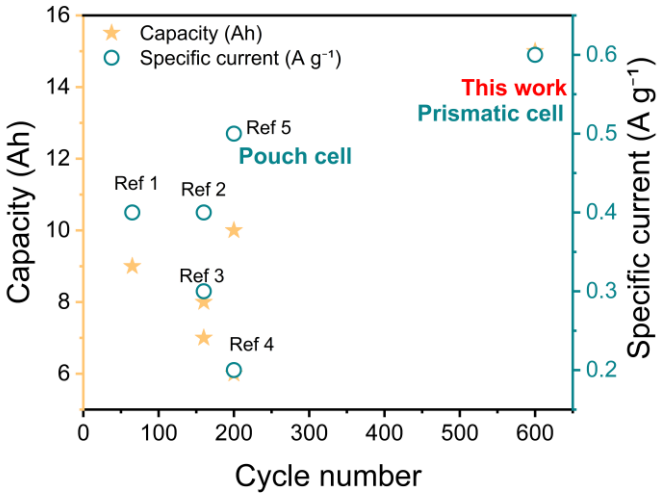

Figure S16 Performance comparison of Zn-based batteries. Comparison of *capacity* (orange stars, left axis) and *specific current* (cyan circles, right axis) versus *cycle number* for representative Zn-based battery systems (Refs. 1–5) and this work. The present Zn-based system exhibits a high practical capacity of **15 Ah** and excellent durability over **600 cycles**, outperforming previous reports in both energy and rate performance.

Reference:

[1]. Li, M. et al. Comprehensive H_2O molecules regulation via deep eutectic solvents for ultra-stable zinc metal anode. *Angew. Chem.* **135**, e202215552 (2023).

[2]. Wang, Y. et al. Manipulating electric double layer adsorption for stable solid-electrolyte interphase in 2.3 Ah Zn-pouch cells. *Angew. Chem.* **135**, e202302583 (2023).

[3]. Hu, N. et al. A double-charged organic molecule additive to customize electric double layer for super-stable and deep-rechargeable Zn metal pouch batteries. *Adv. Funct. Mater.* **34**, 2311773 (2024).

[4]. Qin, H. et al. Achieving high-rate and high-capacity Zn metal anodes via a three-in-one carbon protective layer. J. Mater. Chem. A 10, 17440–17451 (2022).

[5]. Wang, F. et al. Production of gas-releasing electrolyte-replenishing Ah-scale zinc metal pouch cells with aqueous gel electrolyte. *Nat. Commun.* **14**, 4211 (2023).